Iron-oxygen vacancy defect association in polycrystalline iron-modified $PbZrO_3$ antiferroelectrics: Multifrequency electron paramagnetic resonance and Newman superposition model analysis

Hrvoje Meštrić, Rüdiger-A. Eichel,* and Klaus-Peter Dinse
Eduard-Zintl-Institute, Darmstadt University of Technology, D-64287 Darmstadt, Germany

Andrew Ozarowski, Johan van Tol, and Louis Claude Brunel
Center for Interdisciplinary Magnetic Resonance, National High Magnetic Field Laboratory, Florida State University, Tallahassee, Florida 32310, USA

Hans Kungl and Michael J. Hoffmann
Institute of Ceramics in Mechanical Engineering, University of Karlsruhe, D-76131 Karlsruhe, Germany

Kristin A. Schönau, Michael Knapp, and Hartmut Fuess
Materials Science, Darmstadt University of Technology, D-64287 Darmstadt, Germany
(Received 2 November 2005; revised manuscript received 18 January 2006; published 3 May 2006)

By utilizing multifrequency electron paramagnetic resonance (EPR) spectroscopy, the iron functional center in Fe^{3+}-modified polycrystalline lead zirconate ($PbZrO_3$) was studied. The single phase polycrystalline sample remained orthorhombic and antiferroelectric down to 20 K as confirmed by high-resolution synchrotron powder diffraction. The Fe^{3+} ions were identified as substituting for Zr^{4+} at the B-site of the perovskite ABO_3 lattice. Similarly as found for Fe^{3+}:$PbTiO_3$ [Meštrić *et al.*, Phys. Rev. B **71**, 134109 (2005)], the value of the fine-structure (FS) parameter B_2^0 is only consistent with a model in which a charged $(Fe'_{Zr}-V_O^{\bullet\bullet})^{\bullet}$ defect associate is formed. In contrast to a well defined iron functional center in lead titanate ($PbTiO_3$) with FS parameters exhibiting variances of less than 3%, a strong broadening of the EPR powder pattern was observed in lead zirconate, indicating a much larger variance of FS parameters. It is suggested that the apparent broad distribution of fine-structure parameters arises from the system's capability to realize different oxygen vacancy positions in the first coordination shell around the iron site. This proposed model of a small number of distinct iron-oxygen vacancy sites is supported by the observation that corresponding B_2^0 and orthorhombic B_2^2 FS parameters of these sites are anticorrelated, a property not expected for random distributions of fine-structure parameters.

DOI: 10.1103/PhysRevB.73.184105 PACS number(s): 61.72.Ji, 61.72.Bb, 85.50.−n

I. INTRODUCTION

Functional ceramics based on lead zirconate titanate solid solutions ($Pb[Zr_xTi_{1-x}]O_3$, PZT) are the *materials-of-choice* in a wide range of applications.[1–5] One of the key advantages is that material properties may be tailored by adding aliovalent transition-metal or rare-earth ions on a percentage level to these compounds. Because of the low concentration of such functional centers, standard bulk characterization techniques are not well suited for their analysis and electron paramagnetic resonance (EPR) becomes the *method-of-choice* due to its superior sensitivity. Obviously, a reasonable starting point for a detailed analysis of the role of functional centers in the PZT solid solution system is provided by studying first the "pure members" lead titanate ($PbTiO_3$, PT) and lead zirconate ($PbZrO_3$, PZ). Concerning these, PT in its ferroelectric phase has tetragonal and hence higher symmetry than the antiferroelectric PZ, which exists in the more complex orthorhombic structure.

When doping with aliovalent acceptor-type ions, the predominant charge compensation process is the creation of oxygen vacancies ($V_O^{\bullet\bullet}$), which in turn are usually the dominant charge carriers in ceramic oxides. Recent studies have shown that $V_O^{\bullet\bullet}$ either forms an oriented and charged $(Fe'_{Ti}$-$V_O^{\bullet\bullet})^{\bullet}$ defect associate with the iron functional center in PT,[6–8] or provides mobile $V_O^{\bullet\bullet}$ charge carriers in the case of Cu^{2+}-modified PZT compounds.[8–10] For $PbZrO_3$ it is still an open question if either "free" Fe^{3+} and $V_O^{\bullet\bullet}$ defects or associated $(Fe'_{Ti}$-$V_O^{\bullet\bullet})^{\bullet}$ defect dipoles prevail. In order to answer this question it is necessary to precisely determine the Fe^{3+} fine-structure (FS) spin-Hamiltonian parameters.

In this work we report on high-frequency EPR studies of Fe^{3+} functional centers in lead zirconate. The FS interaction induced by the crystal field originating from the nearest-neighbor O^{2-} ions and potentially oxygen vacancies around the Fe^{3+} center provides the possibility for sensitively probing the local symmetry at the dopant site. Considering the ionic radii, the site of incorporation is supposed being the (Zr^{4+}) B-site, similar to PT. An accurate determination of the FS parameters provides a profound basis for local structure modeling by the semiempirical Newman superposition model.[7]

II. EXPERIMENTAL

Lead zirconate, doped with 0.5 mol % iron, was prepared by a mixed oxide route. In order to determine the appropriate weights of the oxide components, the stoichiometry was cal-

culated according to the assumption that iron Fe^{3+} occupies B^{4+}-sites of the perovskite structure. Charge compensation was supposed to be accomplished by oxygen vacancies, corresponding to a chemical composition of the material as $Pb(Zr_{0.995}Fe_{0.005})O_{2.9975}$. Lead oxide (Tetranox, Liebau), zirconia (CS02, SEPR), and iron oxide Fe_2O_3 (Merck) were mixed by attrition milling at 1000 rpm for 3 h in isopropanol. A polyamide crucible, a polyamide stirrer, and YTZ (2 mm) milling balls were used for this process. After separation of the liquid in a rotation distiller, the powder mixture was dried at 100 °C for 48 h and then passed through a metal sieve. The iron doped lead zirconate was then synthesized by calcination at 850 °C for 2 h in a closed alumina crucible. Fine grained ceramic powder was produced by milling using a planetary mill operated at 200 rpm for 6 h. The processing was completed by drying the material for four days and sieving the PZ-Fe powder through a 160 μm mesh.

X-band continuous wave EPR measurements were performed using a Bruker ESP 300E spectrometer with a rectangular TE_{112} resonator. The magnetic field was read out with a nuclear magnetic resonance (NMR) gaussmeter (ER 035M, Bruker). For cryogenic temperatures down to 10 K, a helium-flow cryostat (Oxford) was used. The applied microwave power was 1.5 mW and the field was modulated with a frequency of 100 kHz and amplitude of 0.1 mT. 240 GHz EPR measurements were performed at the National High Magnetic Field Laboratory (NHMFL) on a spectrometer invoking a quasi-optic setup without resonator.[11] Microwave radiation was provided by the multiplied output of a Gunn oscillator. Heterodyne signal detection allowed full control of the signal phase.[12]

The high-resolution synchrotron powder diffraction experiments were carried out in reflection geometry at B2, Hasylab in Hamburg (Germany). The measurement was performed at 20 K in a He closed-cycle cryostat, equilibrating the temperature in a low-pressure helium atmosphere. The powdered sample was glued onto a Si (711) low-background wafer and measured using an incident beam of wavelength $\lambda = 0.049\,925\,6$ nm in combination with an analyzer crystal and a scintillation counter.[13]

III. THEORETICAL DESCRIPTION

The free trivalent iron ion possesses five unpaired electrons in the $3d$ shell ($3d^5$). As the orbital angular momentum is zero, the ground state of the ion is ${}^6S_{5/2}$. In a crystal field, the degeneracy of the Fe^{3+} spin levels is lifted into three Kramers doublets due to internal electric field gradients. The remaining degeneracy may be lifted by an external magnetic field resulting in six Zeeman levels. The corresponding spin-Hamiltonian for this ion may be written as

$$\mathcal{H} = g_e \beta_e \mathbf{B}_0 \cdot \mathbf{S} + \sum_{k=2,3,4,5}^{-k \leqslant q \leqslant k} B_k^q O_k^q(S_x, S_y, S_z) \qquad (1)$$

in which the g-matrix is taken as isotropic with $g_e = 2.0023$ the free electron g-value, β_e denotes the Bohr magneton, $\mathbf{B_0}$ the external magnetic field, B_k^q are the FS spin-Hamiltonian parameters, and O_k^q are the extended Stevens spin operators.[14,15] The standard FS parameters B_k^q are also related to the frequently used parameters b_k^q by the scaling factors f_k ($f_2 = \frac{1}{3}$, $f_4 = \frac{1}{60}$) via $B_k^q = f_k b_k^q$.[14] These values are related to the conventional spectroscopic parameters by $B_2^0 = \frac{b_2^0}{3} = \frac{D}{3}$, $B_2^2 = \frac{b_2^2}{3} = E$, $B_4^4 = \frac{b_4^4}{60} = \frac{5a}{120}$, and $B_4^0 = \frac{b_4^0}{60} = \frac{F}{180} + \frac{a}{120}$.[17,18] As the Zr-site in $PbZrO_3$, at which the Fe^{3+} ion is incorporated, is a general position with site symmetry $1(C_1)$, in principle all conceivable B_k^q parameters, resulting from third-, fourth-, and fifth-rank tensors, have to be considered.[16] All experimentally hitherto observed B_4^q parameters for Fe^{3+} are orders of magnitude smaller than the dominant B_2^q terms. Nevertheless, their influence could be detected in our spectra (see below). The odd-rank tensor contributions are inherently field-dependent. In our multifrequency spectral analysis of the powder spectra, however, we found no evidence for this possible contribution.

For commonly employed *X*-band frequencies, the FS interaction of Fe^{3+} in a distorted or incomplete oxygen octahedron often may be of the same order of magnitude or even larger than the microwave energy quanta ($B_2^q \approx h\nu_{\mathrm{mw}}$). As a result, m_S is not a "good quantum number" and transitions may occur between all levels, depending on their transition probabilities. Thus, a multifold of resonance lines is expected, spanned over a wide field range. In particular, so-called "looping transitions" that do not continue over all possible orientations, and "crossing transitions" that are degenerate at specific orientations are expected.[19] The resulting spectra hence are complicated and, consequently, the determination of FS parameters is not unambiguous.

In order to precisely determine the FS parameters for polycrystalline compounds, the use of microwave frequencies exceeding the FS interaction is mandatory.[6] If the *high-frequency regime* is established ($h\nu_{\mathrm{mw}} \gg B_2^q$), the FS interaction may be treated as a perturbation of the Zeeman levels. The corresponding energy levels are well-separated and m_S becomes a "good quantum number."[20] Consequently, the second-rank FS parameters B_2^q may be directly determined via first-order shifts of the resonance-line positions on the basis of perturbation expressions.[21]

In order to gain relevant structural information from the FS parameters, the B_k^q spin-Hamiltonian parameters may be calculated summing up contributions from particular ligands. In the case of the Fe^{3+} center in $PbZrO_3$, these contributions are generated predominantly from the nearest-neighbor oxygen-ligand surrounding. According to the Newman superposition model (NSM), the parameters can be expressed as the sum over the single oxygen ligands[18]

$$B_k^q = f_k^{-1} \sum_i \bar{b}_k(R_i) K_k^q(\theta_i, \phi_i) \qquad (2)$$

where the single-ligand contribution $\bar{b}_k(R_i)$ obeys a power-law dependence on the distance between the Fe^{3+} and O^{2-} ions according to

$$\bar{b}_k(R_i) = \bar{b}_k(R_0)\left(\frac{R_0}{R_i}\right)^{t_k}. \qquad (3)$$

The coordination factors $K_k^q(\theta_i, \phi_i)$ embody the geometrical arrangement of the ligand oxygens.[22,23] The power-law ex-

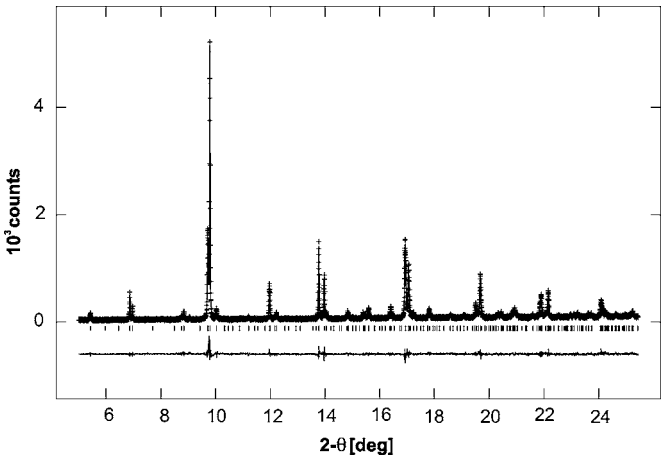

FIG. 1. Observed and calculated diffraction patterns of $PbZrO_3$ obtained from high-resolution synchrotron powder diffraction at 20 K (top) together with its difference curve (bottom). Discrepancies between the observed and calculated diffraction pattern are due to real-structure effects caused by the domain structure of the compound. Wavelength $\lambda = 0.049\,925\,6$ nm.

ponent t_k and the single-ligand contribution $\bar{b}_k(R_0)$ are characteristic for the particular ion-ligand system and have previously been refined empirically.

IV. RESULTS

A. Low-temperature high-resolution powder diffraction measurements of $PbZrO_3$

$PbZrO_3$ undergoes a displacive-type phase transition with temperature, where the paraelectric cubic high-temperature phase changes into an antiferroelectric orthorhombic phase at low temperature via an intermediate phase.[24] This intermediate phase exhibits an additional structural modulation different from the low-temperature structure that forms on heating between 506 and 508 K and on cooling between 508 and 501 K, and which shows the condensation of soft modes.[24]

For many years a discussion about the antiferroelectric or ferroelectric character of the low-temperature phase has been going on. First, a noncentrosymmetric *Pba*2 structure with a polar moment along the [001] direction caused by unbalanced shifts of oxygen atoms has been assumed.[25] This structure is only "antiferroelectric" in its *ab* plane, because all atomic shifts are antiparallel, but should show ferroelectric effects along the *c*-direction. Later, ferroelectric hysteresis effects have been detected in the intermediate phase only, whereas no piezoelectricity in the room-temperature structure has been observed.[26] Furthermore, convergent beam electron diffraction experiments determined the point group to be *mmm* instead of *mm*2,[27] suggesting *Pbam* as a space group with an antiferroelectric character that was supported by neutron diffraction.[28] Later on, a weak ferroelectricity in $PbZrO_3$ at room temperature has been reported.[29] Various subsequent temperature-dependent x-ray and neutron single-crystal and powder diffraction studies of the low-temperature structure determined the structure as centrosymmetric *Pbam*, and as a proper antiferroelectric stable down to 8 K.[30–32] By

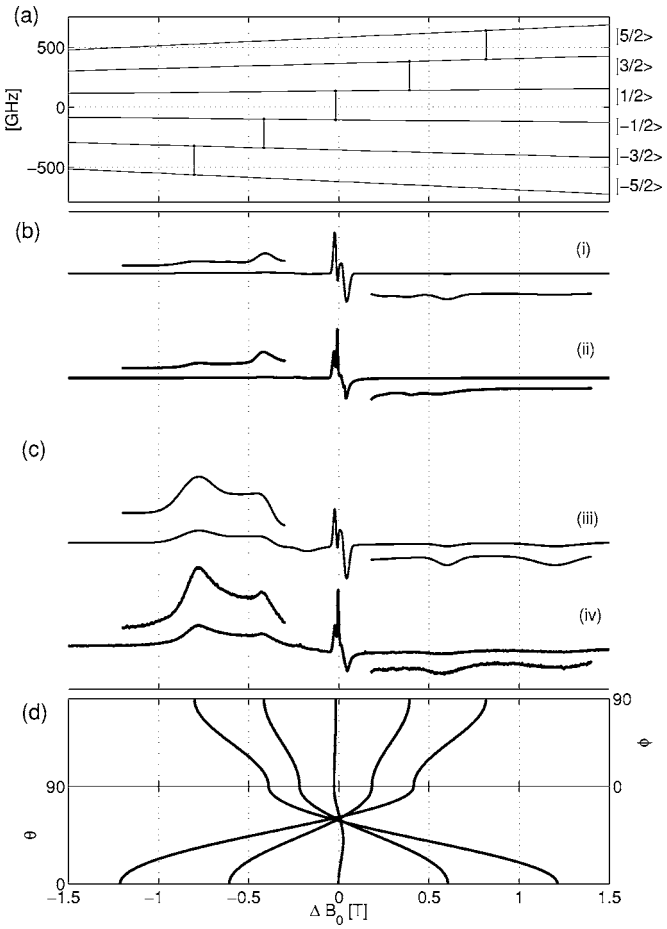

FIG. 2. 240 GHz EPR spectra of Fe^{3+}:$PbZrO_3$ (ii,iv), compared to numerical spectrum simulations (i,iii). (a) Energy level scheme assuming the external field along the *y*-axis ($\theta = \phi = 90°$) with indicated "allowed" ($\Delta m_S = \pm 1$) EPR transitions at 240 GHz. (b) and (c) EPR spectra at 15 and 4.8 K. (d) Orientation dependence of resonance lines for the polar angles (ϕ, θ) relative to the external field orientation.

combining neutron experiments with a pair distribution function modeling (PDF) it could be demonstrated that the Pb atoms are also displaced in the *c*-direction, additionally to the antiparallel shifts within the *ab* plane.[30] This shift increases with increasing temperature and is most probably the origin of the small *c*-axis polarization detected.[29]

In order to obtain precise structural data for the interpretation of the EPR FS parameters at low temperature, high-resolution synchrotron powder diffraction has been performed. The data recorded were subjected to Rietveld refinement using the general structure analysis system (GSAS).[33] After adjustment of the scale factor and peak shape using a pseudo-Voigt function in combination with asymmetry correction,[34] the unit-cell parameters, atomic positions, and thermal displacement parameters of each atom were refined individually. The best fit, shown in Fig. 1, was achieved with the structural model of the centrosymmetric space group *Pbam*, confirming recent results.[30–32] Unit-cell parameters and atom coordinates obtained agree within standard deviations with the ones determined earlier[30,32] and are given in Table I.

TABLE I. Lattice parameters [$a=587.149(10)$ pm, $b=1177.186(18)$ pm, $c=819.614(12)$ pm], cell volume [0.566 504(16) nm^3] and relative atom coordinates for $PbZrO_3$ at 20 K, obtained from high-resolution synchrotron powder diffraction. U_i is the mean square of atomic displacement. Its fluctuation linked to shifts in the oxygen positions can partly be explained by the influence of real structure effects on peak profiles.

Atom	x	y	z	$U_i \cdot 100$	Site symmetry	Wyckoff position
Pb1	0.7083(9)	0.1293(4)	0.000 000	1.42(15)	m	4g
Pb2	0.7032(10)	0.1236(4)	0.500 000	2.94(18)	m	4h
Zr	0.2438(4)	0.1215(8)	0.2489(11)	1.50(7)	1	8i
O1	0.2556(72)	0.1287(73)	0.500 000	2.24(31)	m	4h
O1′	0.3099(86)	0.0973(39)	0.000 000	2.24(31)	m	4g
O2	0.0346(27)	0.2578(16)	0.245(11)	2.24(31)	1	8i
O3	0.000 000	0.500 000	0.318(5)	2.24(31)	2	4f
O4	0.000 000	0.000 000	0.250(19)	2.24(31)	2	4e

B. Multifrequency EPR

The high-frequency EPR spectra at 240 GHz for two different temperatures of Fe^{3+}-modified $PbZrO_3$ are presented in Figs. 2(b) and 2(c). They are dominated by the central $|-\frac{1}{2}\rangle \leftrightarrow |+\frac{1}{2}\rangle$ transition. The outer spectral features originate from transitions $|-\frac{5}{2}\rangle \leftrightarrow |-\frac{3}{2}\rangle$, $|-\frac{3}{2}\rangle \leftrightarrow |-\frac{1}{2}\rangle$, $|+\frac{1}{2}\rangle \leftrightarrow |+\frac{3}{2}\rangle$ and $|+\frac{3}{2}\rangle \leftrightarrow |+\frac{5}{2}\rangle$ [Fig. 2(d)], which are orientation-dependent in first order. The most prominent among these is the $|-\frac{5}{2}\rangle \leftrightarrow |-\frac{3}{2}\rangle$ transition with resonance lines at field offsets $\Delta B_0 = -0.80(9)$ T and $\Delta B_0 = 1.26(7)$ T from the central line at $B_0 = 8.567$ T ($g=2.002$). Further EPR signals at fields $\Delta B_0 = -0.43(9)$ T and $\Delta B_0 = 0.53(2)$ T arise from the $|-\frac{3}{2}\rangle \leftrightarrow |-\frac{1}{2}\rangle$ transition, and the $|+\frac{1}{2}\rangle \leftrightarrow |+\frac{3}{2}\rangle$ transition that already has a comparatively small intensity at 4.8 K [$\Delta B_0 = 0.38(5)$ T]. The remaining $|+\frac{3}{2}\rangle \leftrightarrow |+\frac{5}{2}\rangle$ transition is not observed at this temperature. The width of the central $|-\frac{1}{2}\rangle \leftrightarrow |\frac{1}{2}\rangle$ transition is typically affected by second-order effects, the width being proportional to $(B_2^0)^2/B_0$.[8]

The absence of certain resonance lines may be explained by considering spin-level populations in thermal equilibrium. Whereas at room temperature line intensities are expected exhibiting inversion symmetry with respect to the central line, at 4.8 K ($k_B T \approx 100$ GHz) a significant absolute difference in level populations is only obtained for the two states of lowest energy.[6,37] The corresponding change in line intensities when going to a higher temperature (15 K) can nicely be observed, as shown in Fig. 2(b).

In contrast to the *high-frequency-regime* 240 GHz spectra that are straightforward to interpret, the *low-frequency-regime* *X*-band EPR spectra shown in Fig. 3 consist of transitions that exhibit a complicated orientation dependence with turning points that do not necessarily correspond to canonical orientations. The complete set of FS parameters can thus only be obtained by a simultaneous multifrequency numerical spectrum simulation. The corresponding simulation procedure was based on a numerical diagonalization of the spin Hamiltonian, using two independent software packages[35,36] in order to increase the reliability of the simulation routines.

When tackling the problem of numerical simulation for the *X*-band spectrum, it is observed that the spectral "peak-to-peak" line widths of $\Delta B_{pp}^{PZ} = 12.7$ mT are considerably broader than those for iron-modified lead titanate of $\Delta B_{pp}^{PT} = 3.5$ mT.[6] A conventional description of this situation assumes a single set of FS parameters subjected to a statistical distribution (FS-strain), as schematically illustrated in Fig. 4. Different strain values of $\delta B_2^0 = 0.1$ GHz and $\delta B_2^2 = 0.8$ GHz for the *X*-band spectrum [Fig. 3(iv)] and $\delta B_2^0 = 1.8$ GHz and $\delta B_2^2 = 0.8$ GHz for the 240 GHz spectrum (Fig. 2) had to be used to obtain good agreement with the experimental spectra. By these values the respective full width half maximum of a Gaussian distribution is denoted. Calculated spectra are shown superimposed to both experimental spectra and show good agreement. However, it was not possible to simulate the spectra obtained at different microwave frequencies with a single set of FS-strain values, which would have to be expected, as the FS interaction does not scale with the external field. Consequently, an alternative approach was developed.

By anticipating a correlated oxygen vacancy, a physically more appropriate description invokes the six different distances of the surrounding oxygen ions as given by the crystal structure. Hence, six positions for an oxygen vacancy exist, for which reason six different $(Fe'_{Zr}-V_O^{\bullet\bullet})^{\bullet}$ defect dipoles may be formed. Without further knowledge, in the simulation we allowed contributions from all six sites, even though at low temperature only a subset will be occupied depending on the various site energies. Corresponding density-funtional theory calculations are in progress, in order to further clarify this point. In contrast, for $Fe^{3+}:PbTiO_3$ it has been shown that oxygen vacancies are found only in direction of the crystallographic *c*-axis when seen from the Fe^{3+} position, yielding $(Fe'_{Ti}-V_O^{\bullet\bullet})^{\bullet}$ defect dipoles strictly oriented along the *c*-axis.[7] In order to account for this difference, for $Fe^{3+}:PbTiO_3$ a set of six constituent EPR spectra was assumed with varying FS parameters (cf. Table II). The range of values was chosen as to confirm the widths of the continuous distributions used for simulation of the 240 GHz spectrum. Two spectra of this set are depicted in Figs. 3(i,v) together with the sum of all six EPR spectra [Fig. 3(ii)]. Best results were obtained, when using a set of parameters displaced by equal amounts around the respective mean values. Good agreement with the experimental spectra could only be obtained, if the set of FS parameters exhibits an *anticorrelation* between the shift of B_2^0

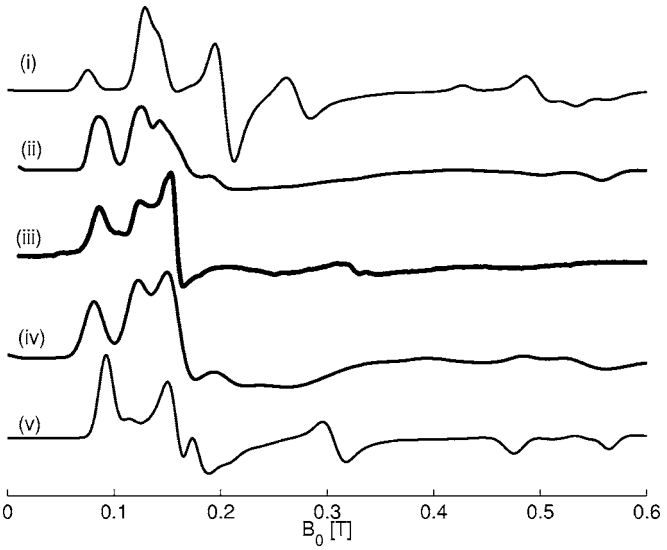

FIG. 3. X-band EPR spectra of Fe^{3+}:$PbZrO_3$ (iii), compared to numerical spectrum simulations. (i,v) Numerical spectrum simulations invoking extreme values of the FS parameters (cf. Table II). (ii) Numerical spectrum simulation with the sum over the six basic EPR spectra taken with equal weight. (iv) Numerical spectrum simulation assuming a single-site model with large FS-strain.

and B_2^2 values as listed in Table II. To show that this anticorrelation is essential for a correct reproduction of the multifrequency EPR spectra, simulations invoking a positive correlation of deviations from an average value instead are also shown. As can be seen in Figs. 5 and 6, the assumed anticorrelation is clearly favored. As a consequence, the Fe^{3+} center in $PbZrO_3$ has to be described by a distinct set than by

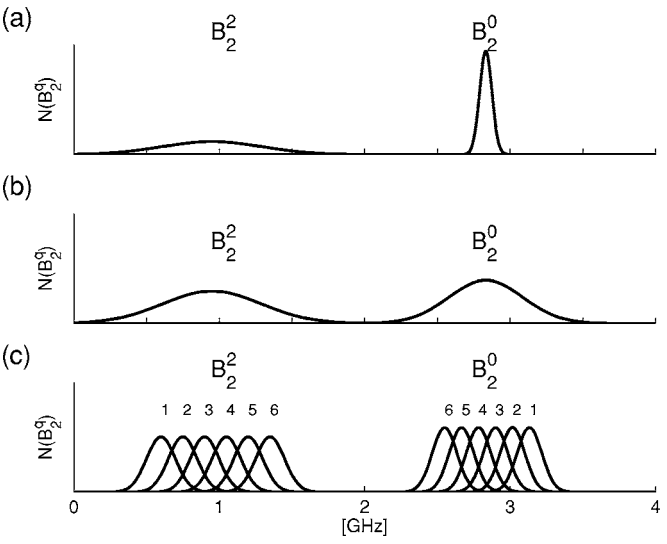

FIG. 4. Schematic representation of the distribution of FS parameters used for spectral simulation. (a) and (b) Single-site model necessitating the use of large strain values (full width half maximum of a Gaussian distribution) of δB_2^0=0.1 GHz, δB_2^2=0.8 GHz for the *X*-band (a) and δB_2^0=1.8 GHz, δB_2^2=0.8 GHz for the 240 GHz case (b). (c) Multi-site model invoking a basis set of six different sites with identical strain values δB_2^0=0.20 GHz and δB_2^2 =0.23 GHz used for simulation at all mw frequencies.

TABLE II. FS parameters for the basis set of six constituent EPR spectra, used for the numerical spectrum simulation of the Fe^{3+}:$PbZrO_3$ EPR spectra. The distributions of parameters of individual spectra amount to δB_2^0=200 MHz and δB_2^2=230 MHz.

Center	B_2^0 (GHz)	B_2^2 (GHz)	B_2^2/B_2^0
1	3.13	0.55	0.19
2	3.02	0.71	0.25
3	2.09	0.87	0.31
4	2.78	1.03	0.38
5	2.67	1.19	0.45
6	2.55	1.35	0.53

a broad distribution (FS-strain). Experimentally it could not be proven that only six distinct centers are involved; however, by considering the crystal structure this seems to be an obvious assumption. For comparing with Fe^{3+} centers in different crystals, the mean values B_2^0=2.8(3) GHz [b_2^0 =8.5(9) GHz], B_2^2=0.95(40) GHz [b_2^2=2.8(12) GHz], B_4^0 =2(2) MHz [b_4^0=120(120) MHz], and B_4^4=8(5) MHz [b_4^4 =48(30) MHz], with a ratio of B_2^2/B_2^0=0.3(2) may be considered as representative.

As compared to previous studies of Fe^{3+} in $PbTiO_3$,[6] in which B_2^0=11.7(6) GHz [b_2^0=35.2(8) GHz] was found, we note that the size of FS interaction in $PbZrO_3$ is considerably smaller, which may be traced back to the significantly reduced distortion of the oxygen octahedron in the bulk $PbZrO_3$ structure. It may further be compared to previous *X*-band results reported for a Fe^{3+} impurity center in a $PbZrO_3$ single crystal,[38] where only the ratio of the second-rank spin Hamiltonian parameters could be determined. In this study, four axial Fe^{3+} centers with identical ratio B_2^2/B_0^2=−0.138, but of different orientations were assumed. For two of the centers the orientations were close to the pseudocubic $[100]_c$ direction, whereas the other two were in the pseudocubic $[010]_c$ direction. However, the reported B_2^2/B_0^2-ratio of this study considerably differs from our result.

C. Newman superposition modeling

Exploiting the determined set of FS parameters, the local structure at the Fe^{3+} functional center may be modeled with the help of the semiempirical Newman superposition model.[18] The intrinsic NSM parameters t_2 and $\bar{b}_2(R_0)$ were adopted from similar single crystal studies having equivalent Fe^{3+}–O^{2-} bonds in octahedral coordination. For Fe^{3+} in MgO, the set of NSM parameters determined is $\bar{b}_2$= −12.3514 GHz, t_2=8, and R_0=210.1 pm.[39,40] For our calculations, the nearest-neighbor oxygen positions were taken from the x-ray data at 20 K (Sec. IV A). The coordinate system for the NSM calculation was chosen identical to the crystal coordinate system. Finally, the FS tensor was transformed into its eigenframe.

The unit cell of lead zirconate contains $4\times2\times2$ distorted pseudocubic perovskite cells, for which the orthorhombic lattice parameters (a,b,c) are related to the pseudocubic pa-

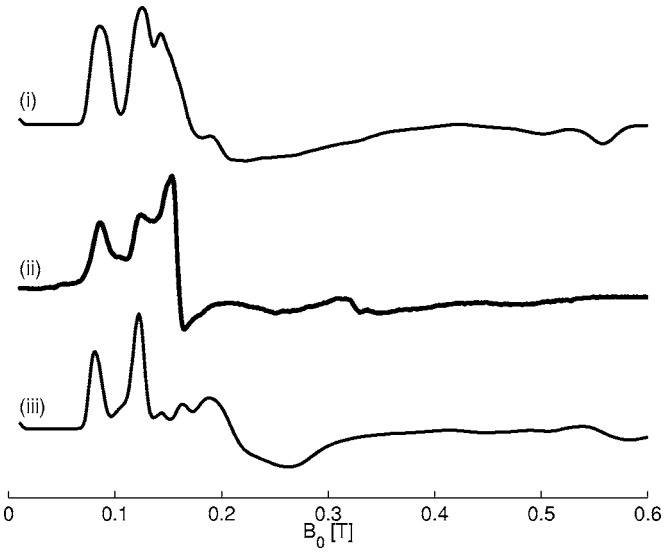

FIG. 5. X-band EPR spectra of Fe^{3+}:$PbZrO_3$ (ii) as compared to simulations assuming a six-site model. (iii) Correlation and (i) anticorrelation of the FS-parameters B_2^0 and B_2^2.

rameters (a_c, b_c, c_c) via $a=2a_c\cos(\pi/4)$, $b=4b_c\cos(\pi/4)$, and $c=2c_c$. In the low-temperature (antiferroelectric) phase, the Pb atoms are shifted antiparallel from the ideal perovskite positions in direction $[1\bar{1}0]_c$, the O^{2-} octahedra are rotated about the $[1\bar{1}0]_c$ axis and the Zr atoms are marginally displaced along $[001]_c$ of the pseudocubic coordinate system [Fig. 7(a)]. As all four Zr^{4+} sites may be described by the same Wyckoff position (8*i*), the arrangement of the oxygen ligands is identical for all the Zr^{4+} positions in the unit cell and thus only a single oxygen octahedron has to be taken into consideration [Fig. 7(b)], as the influence of the lead ions is neglected in the NSM analysis.

In order to decide if an oxygen vacancy occurs in the first coordination sphere of the iron center or if charge compensation occurs in a more distant sphere, two structural models were investigated, with and without an oxygen vacancy in the nearest-neighbor position of the Fe^{3+} center. Because in pure $PbZrO_3$ all Zr-O distances differ (Table III) and because the determined symmetry of the FS tensor imposes no constraints on the orientation of a $(Fe'_{Zr}-V_O^{\bullet\bullet})^{\bullet}$ defect dipole, the model of a directly coordinated oxygen vacancy can be realized in six different arrangements, $V_O^{\bullet\bullet}$ possibly substituting for each of the ligand oxygens (Fig. 7). The positions of the oxygen ligands in the local octahedron are defined by the crystal coordinate system given in Table I. Parameters B_2^0 and B_2^2 were calculated varying the position of Fe^{3+} along the line connecting its initial position with the respective oxygen position. The distance d is defined as the shift of the Fe_{Zr}^{3+} along this line, a positive sign of d denoting a shift towards the oxygen vacancy.

In Fig. 8, the calculated FS parameters B_2^0 and B_2^2 as functions of the distance d for two of the structural models, invoking an oxygen vacancy substituted at the shortest Fe-O distance [O2′(2) at 205.5 pm] and for the longest distance [O2′(1) at 217.7 pm], are depicted. For comparison, the experimentally obtained values for B_2^0 and B_2^2 are represented by solid horizontal lines. Because there is no way to relate one of the assumed six EPR spectra to a certain structural model, dashed horizontal lines indicate the range of B_2^0 and B_2^2 spanned by the constituent EPR spectra (Table II). The observed jumps in the calculated dependence of B_2^0 can be rationalized by realizing that the displacement of the iron ion is not necessarily along a symmetry axis. In both models, agreement with the experimental data can only be obtained by an $(Fe'_{Zr}-V_O^{\bullet\bullet})^{\bullet}$ defect associate, because the model invoking a complete octahedron does not reproduce the experimental value regardless of displacement d. Obviously, the measured positive sign of B_2^0 turns out to be decisive for this analysis. For reason of completeness, NSM calculations invoking substitutions of $V_O^{\bullet\bullet}$ at the remaining oxygen positions were also performed, confirming the formation of an $(Fe'_{Zr}-V_O^{\bullet\bullet})^{\bullet}$ defect dipole. The corresponding results are compiled in Table III. Consequently, an oxygen vacancy substituting at any of the six nearest-neighbor oxygen sites reproduces the experimental value of B_2^0.

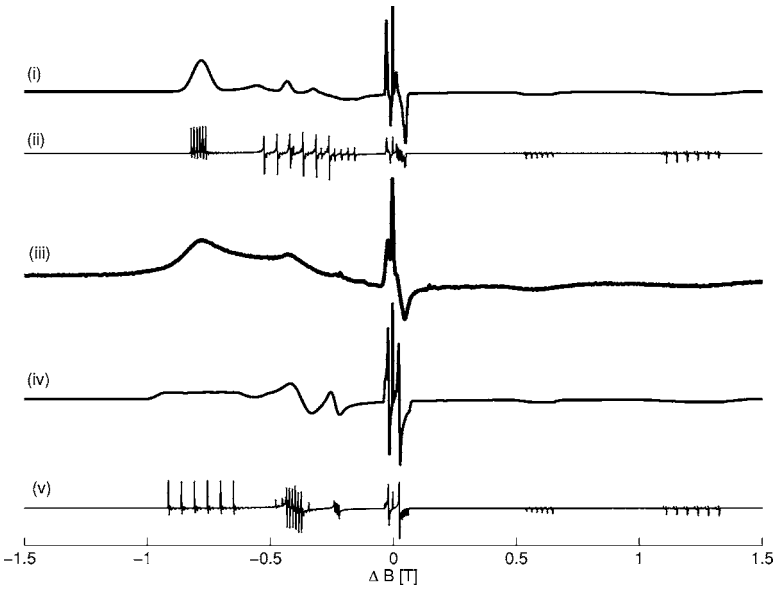

FIG. 6. 240 GHz EPR spectra of Fe^{3+}:$PbZrO_3$ (iii) as compared to simulations assuming a six-site model. (iv,v) Correlation and (iv) anticorrelation of the FS parameters B_2^0 and B_2^2. The "stick-spectra" (ii,v) show the superposition of all six constituent EPR spectra.

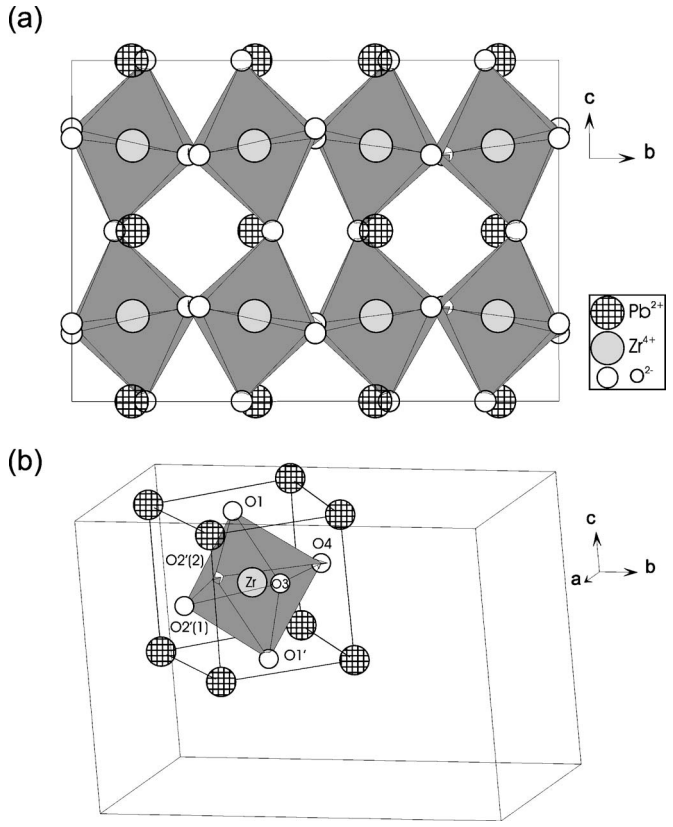

FIG. 7. (a) Unit cell of $PbZrO_3$. (b) Oxygen octahedron of $PbZrO_3$ selected for Newman superposition calculations.

Concerning the resulting displacements of the Fe'_{Zr} center as compared to the $Zr^{\times}_{Zr}$ position, the B_2^0 calculations predict two possible displacements (d_1 and d_2). By taking into account the additional information provided by the NSM calculations of B_2^2, as shown in Figs. 8(c) and 8(d), a slight shift of d_2 in opposite direction of the oxygen vacancy towards the remaining pyramid of oxygen ions is clearly favored over the situation in which the Fe'_{Zr} center is considerably more displaced by d_1 towards the oxygen vacancy. Qualitatively, this result corresponds to the situation in $PbTiO_3$, for which comparable displacements of the Fe'_{Ti} center with respect to the $Ti^{\times}_{Ti}$ position have been observed.[7]

Owing to the large unit-cell size of $PbZrO_3$, density functional theory (DFT) calculations are not available, so that the effect of relaxed positions of the oxygen ions towards the oxygen vacancy in the NSM calculation could not be considered.

V. DISCUSSION

The most important information obtained from the NSM calculations is that the Fe^{3+} functional center in lead zirconate forms a charged $(Fe'_{Zr}-V_O^{\bullet\bullet})^{\bullet}$ defect associate with an oxygen vacancy in the local oxygen octahedron, similar to the situation found in Fe^{3+}-modified lead titanate,[6–8] but contrary to experimental findings for other acceptor centers, like chromium-doped $PbTiO_3$[41] and copper-modified $Pb[Zr_{0.54}Ti_{0.46}]O_3$,[8–10] for which no such association is present. With respect to the ionic mobility of "free" oxygen vacancies, the iron-oxygen vacancy defect dipole complex will therefore be rather immobile in the ceramic, considerably hindering charge transport in the compound. Furthermore, the charged defect associate may influence the poling properties by providing pinning centers for domain walls.[42,43] In particular, oxygen-vacancy related defect dipoles have been shown to be involved in voltage offsets leading to imprint failure[44] and are suggested to play a crucial role in electrical fatigue.[45–47]

Second, contrary to the *single-site* $PbTiO_3$ case, for which a single orientation of the $(Fe'_{Ti}-V_O^{\bullet\bullet})^{\bullet}$ dipole was observed, the obtained result points to a *multi-site* situation in $PbZrO_3$, generated by different possible orientations of the $(Fe'_{Zr}-V_O^{\bullet\bullet})^{\bullet}$ dipole owing to the fact that the oxygen vacancy may take several or all of the nearest-neighbor oxygen sites in $PbZrO_3$. This assignment is supported by results obtained for the Cu^{2+} center in $PbZrO_3$ that is not associated to an oxygen vacancy.[8] Here, the EPR lines for Cu^{2+}-modified $PbZrO_3$ are not broadened as compared to Cu^{2+}:$PbTiO_3$.[8] Consequently, the $(Fe'_{Zr}-V_O^{\bullet\bullet})^{\bullet}$ dipole is expected to reorient easier in lead zirconate as compared to lead titanate. Thus, the above mentioned effects of domain-wall clamping most probably are reduced for iron-modified lead zirconate as compared to lead titanate.

As the $V_O^{\bullet\bullet}$ are associated to Fe^{3+} centers, any clustering of oxygen vacancies seems to be rather unlikely. However, such defect clusters have been proposed to exist related to localized polaron states, as which the majority of electron states

TABLE III. Possible positions (in pm) of the Fe^{3+} ion resulting from the NSM calculations of the B_2^0 and B_2^2 parameters for the $(Fe'_{Zr}-V_O^{\bullet\bullet})^{\bullet}$ center compared to experimental values. The calculations were performed for $V_O^{\bullet\bullet}$ replacing a particular oxygen in the octahedron and locating it along the line of the previous Zr-O bond (cf. Fig. 7).

$V_O^{\bullet\bullet}$ position	Zr-O length	From B_2^0		From B_2^2	
		d_1	d_2	d_1	d_2
O1	206.1	−10(6)	75(5)	−12(5)	—
O1′	209.6	−10(6)	64(5)	13(10)	95(7)
O2′(1)	222.2	−2(6)	94(5)	−14(4)	—
O2′(2)	202.1	−23(5)	64(5)	7(15)	—
O3	215.2	−2(6)	82(5)	−2(6)	—
O4	202.4	−10(6)	70(5)	−28(10)	50(30)

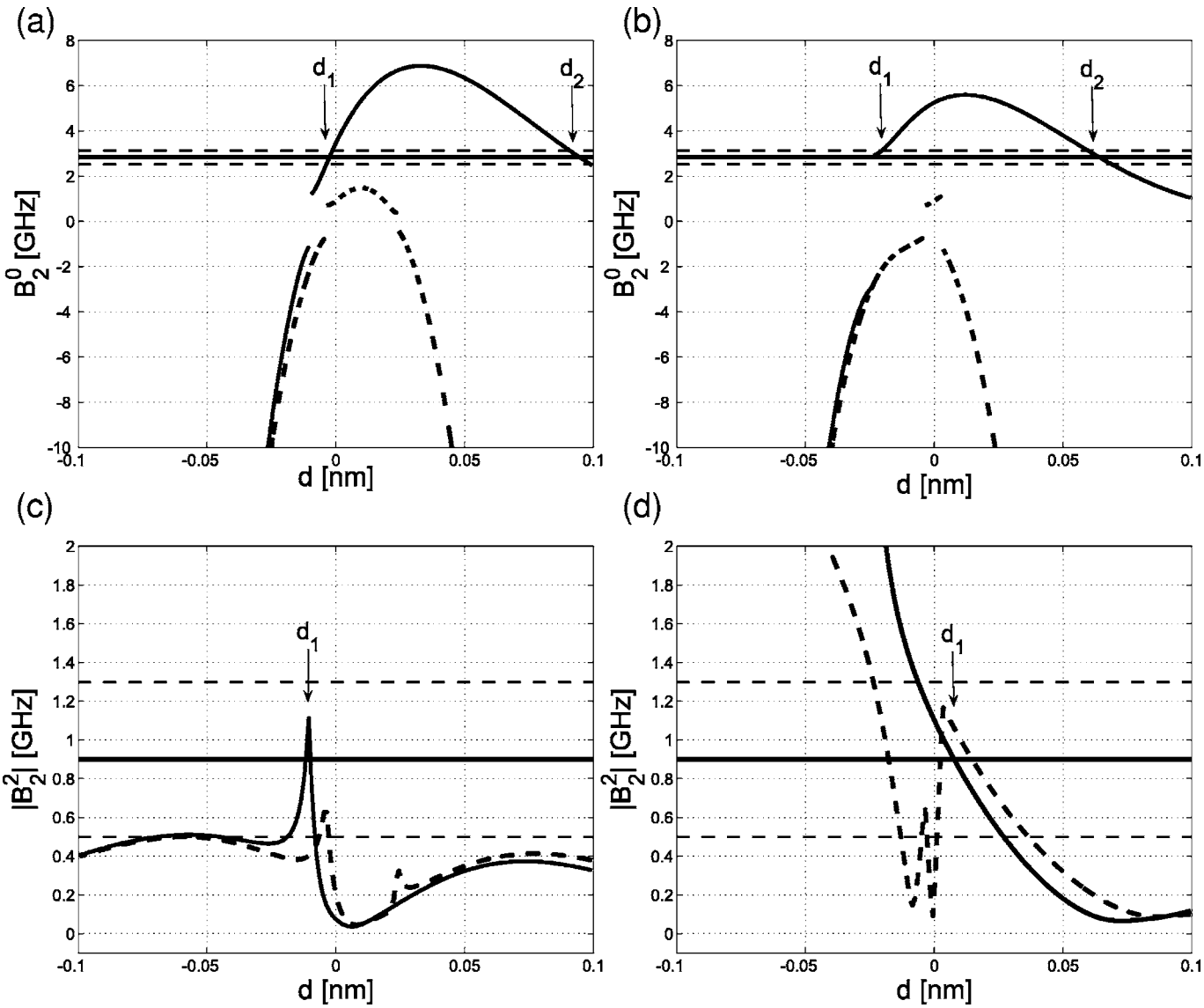

FIG. 8. Newman superposition calculations for B_2^0 (a) and (b) and B_2^2 (c) and (d) for $Fe^{3+}:PbZrO_3$. (a) and (c) Oxygen vacancy at position O2′(1). (b) and (d) Oxygen vacancy at position O2′(2). The solid horizontal lines represent the experimental mean values for B_2^0 and B_2^2, and the dashed horizontal lines mark the range of values for B_2^0 and B_2^2 spanned by the six constituent EPR spectra. The full line represents the Newman superposition calculations with an associated oxygen vacancy, and the dashed lines stand for calculations assuming a complete octahedron. The distance d is defined according to a line connecting O^{2-} and the original Zr^{4+} position, with the positive direction towards the O^{2-} position.

in perovskite oxides have been identified, promoting only a small fraction of electrons into the conduction band.[48] Owing to the observed $(Fe'_{Zr}-V_O^{\bullet\bullet})^{\bullet}$ association and the consequently reduced mobility of $V_O^{\bullet\bullet}$, this hypothesis hence cannot be upheld for iron-modified lead titanate and zirconate.

The mechanism of charge compensation for this compound may be discussed analogously to $Fe^{3+}:PbTiO_3$,[7] assuming that partial charge compensation takes place at a nearest-neighbor oxygen site in the octahedron. Furthermore, exclusively charged $(Fe'_{Zr}-V_O^{\bullet\bullet})^{\bullet}$ associates are formed, excluding the existence of free Fe^{3+} ions without associated $V_O^{\bullet\bullet}$. Overall charge compensation is proposed being accomplished by double negatively charged lead vacancies V''_{Pb}

$$[V_O^{\bullet\bullet}] = [Fe'_{Zr}] + \frac{1}{2}[V''_{Pb}]. \quad (4)$$

In principle, charge-compensation could also be obtained by more complex $(Fe'_{Zr}-V_O^{\bullet\bullet}-Fe'_{Zr})^{\times}$ defect associates without the need for lead vacancies at all. However, the present EPR experiment gives no evidence for this hypothesis, because no indication for strongly dipolar coupled iron centers is detected, for which reason this model is discarded.

Concerning the reliability of the predictions obtained by the semiempirical NSM approach, the following points should be mentioned. Although for iron-modified lead titanate the NSM approach provides results in agreement with

DFT calculations,[7] it should be remembered that crystal distortions near the substituted ion and contributions from ions or vacancies more distant than neighboring ligands are neglected. Furthermore, the model is based upon the calculation of single electron-derived charge densities, whereas the FS interaction is related to two-electron expectation values. However, the NSM was proven to yield reliable results for determining the second- and fourth-rank FS parameters in *S*-state ions, since the intrinsic parameters have been refined over several decades using a large set of experimental data.

Because of the present lack of DFT optimized structures, "ideal" positions for the oxygens had to be invoked rather than relaxed positions for the NSM calculations.[49] As has been shown for Fe^{3+}:$PbTiO_3$, oxygen ions will relax towards the vacancy. Whereas the relaxation of oxygen ions will most probably not influence the qualitative assignment of the $(Fe'_{Zr}-V_O^{\bullet\bullet})^{\bullet}$ defect formation, use of relaxed oxygen positions is mandatory for more than a qualitative determination of the displacement of the Fe^{3+} ion.[7] The formation of a charged $(Fe'_{Zr}-V_O^{\bullet\bullet})^{\bullet}$ defect dipole, however, can be taken as a reliable result of the present NSM calculations, whereas the determined Fe^{3+} displacement has to be considered as rather rough estimate.

VI. CONCLUSION

In summary, the present multifrequency EPR analysis has allowed for an identification of a charged $(Fe'_{Zr}-V_O^{\bullet\bullet})^{\bullet}$ defect associate in iron-modified $PbZrO_3$. Its microscopic structure is characterized on the basis of semiempirical NSM calculations. In the model presented, Fe^{3+} is substituted as an acceptor center at the perovskite B-site with a directly coordinated oxygen vacancy. Contrary to the situation in $PbTiO_3$, there is no preferred site of the oxygen vacancy and hence no preferred orientation of the related charged $(Fe'_{Zr}-V_O^{\bullet\bullet})^{\bullet}$ defect dipole. Using high-resolution synchrotron powder diffraction, it was verified that lead zirconate remains orthorhombic and antiferroelectric down to 20 K.

The impact of iron-doping in lead zirconate on the macroscopic piezoelectric properties can thus be rationalized from a microscopic point of view, because the location of the iron-oxygen vacancy defect dipole complex within the lattice will be rather immobile in the ceramic as compared to the ionic mobility of free oxygen vacancies. Thus, charge transport will be considerably hindered and the charged defect agglomerate may furthermore influence domain-wall motion and poling properties by providing pinning domain walls. On the other hand, the identification of a multisite iron center with different orientations of the $(Fe'_{Zr}-V_O^{\bullet\bullet})^{\bullet}$ defect dipole points to an easier reorientation of that dipole in lead zirconate as compared to the situation in lead titanate, where the $(Fe'_{Ti}-V_O^{\bullet\bullet})^{\bullet}$ dipole is strictly oriented along the crystallographic *c*-axis.

ACKNOWLEDGMENTS

This research has been financially supported by the DFG priority program 1051 "High-Field EPR in Biology, Chemistry, and Physics" and center of excellence 595 "Electrical Fatigue in Functional Materials." The NHMFL is supported by the NSF through Grant No. DMR9016241.

*Corresponding author. FAX: +49-6151-164347. Email address: eichel@chemie.tu-darmstadt.de

[1] B. Jaffe, W. R. Cook, and H. Jaffe, *Piezoelectric Ceramics* (Academic, London, 1971).
[2] Y. Xu, *Ferroelectric Materials and Their Applications* (Elsevier, Amsterdam, 1991).
[3] K. Uchino, *Ferroelectric devices* (Dekker, New York, 2000).
[4] M. E. Lines and A. M. Glass, *Principles and Applications of Ferroelectrics and Related Materials* (Oxford University Press, Oxford, 2001).
[5] S. Sugihara, T. Bak, J. Nowotny, M. Radecka, and C. C. Sorrell, J. Mater. Synth. Process. **6**, 335 (1998).
[6] H. Meštrić, R.-A. Eichel, K.-P. Dinse, A. Ozarowski, J. van Tol, and L. C. Brunel, J. Appl. Phys. **96**, 7440 (2004).
[7] H. Meštrić, R.-A. Eichel, T. Kloss, K.-P. Dinse, S. Laubach, S. Laubach, P. C. Schmidt, K. A. Schonau, M. Knapp, and H. Ehrenberg, Phys. Rev. B **71**, 134109 (2005).
[8] R.-A. Eichel, H. Meštrić, K.-P. Dinse, A. Ozarowski, J. van Tol, L. C. Brunel, H. Kungl, and M. J. Hoffmann, Magn. Reson. Chem. **43**, S166 (2005).
[9] R.-A. Eichel, H. Kungl, and M. J. Hoffmann, J. Appl. Phys. **95**, 8092 (2004).
[10] R.-A. Eichel, K.-P. Dinse, H. Kungl, M. J. Hoffmann, A. Ozarowski, J. van Tol, and L. C. Brunel, Appl. Phys. A: Mater. Sci. Process. **80**, 51 (2005).
[11] A. K. Hassan, L. A. Pardi, J. Krzystek, A. Sienkiewicz, P. Goy, M. Rohrer, and L. C. Brunel, J. Magn. Reson. **142**, 300 (2000).
[12] J. van Tol, L. C. Brunel, and R. J. Wylde, Rev. Sci. Instrum. **76**, 074101 (2005).
[13] M. Knapp, C. Baehtz, H. Ehrenberg, and H. Fuess, J. Synchrotron Radiat. **11**, 328 (2004).
[14] A. Abragam and B. Bleaney, *Electron Paramagnetic Resonance of Transition Ions* (Clarendon Press, Oxford, 1970).
[15] C. Rudowicz, Magn. Reson. Rev. **13**, 1 (1987).
[16] V. G. Grachev, Sov. Phys. JETP **65**, 1029 (1987).
[17] C. Rudowicz and S. Madhu, J. Phys.: Condens. Matter **11**, 273 (1999).
[18] D. J. Newman and Betty Ng, Rep. Prog. Phys. **52**, 699 (1989).
[19] K. S. Misra, J. Magn. Reson. **137**, 8392 (1999).
[20] J. R. Pilbrow, *Transition Ion Electron Paramagnetic Resonance* (Clarendon, Oxford, 1990).
[21] B. V. R. Chowdari and P. Venkateswarlu, J. Chem. Phys. **48**, 318 (1968).
[22] C. Rudowicz, J. Phys. C **18**, 1415 (1985).
[23] S. C. Chen and D. J. Newman, Aust. J. Phys. **35**, 133 (1982).
[24] H. Fujishita and S. Hoshino, J. Phys. Soc. Jpn. **53**, 226 (1984).
[25] F. Jona, G. Shirane, F. Mazzi, and R. Pepinsky, Phys. Rev. **105**, 849 (1957).

[26] B. A. Scott and G. Burns, J. Am. Ceram. Soc. **55**, 331 (1972).
[27] M. Tanaka, R. Saito, and K. Tsuzuki, Jpn. J. Appl. Phys., Part 1 **21**, 291 (1982).
[28] H. Fujishita, Y. Shiozaki, N. Achiwa, and E. Sawaguchi, J. Phys. Soc. Jpn. **51**, 3583 (1982).
[29] X. Dai, J.-F Li, and D. Viehland, Phys. Rev. B **51**, 2651 (1995).
[30] S. Teslic and T. Egami, Acta Crystallogr., Sect. B: Struct. Sci. **54**, 750 (1998).
[31] D. L. Corker, A. M. Glazer, J. Dec, K. Roleder, and R. W. Whatmore, Acta Crystallogr., Sect. B: Struct. Sci. **53**, 135 (1997).
[32] H. Fujishita, Y. Ishikawa, S. Tanaka, A. Ogawaguchi, and S. Katano, J. Phys. Soc. Jpn. **72**, 1426 (2003).
[33] A. C. Larson and R. B. Von Dreele, General Structure Analysis System (GSAS), Los Alamos National Laboratory Report LAUR (2004), pp. 86–748.
[34] L. W. Finger, D. E. Cox, and A. P. Jephcoat, J. Appl. Crystallogr. **27**, 892 (1994).
[35] G. R. Hanson, K. E. Gates, C. J. Noble, M. Griffin, A. Mitchell, and S. Benson, J. Inorg. Biochem. **98**, 903 (2004).
[36] S. Stoll and A. Schweiger, J. Magn. Reson. **178**, 42 (2006).
[37] R.-A. Eichel, H. Meštrić, H. Kungl, and M. J. Hoffmann, Appl. Phys. Lett. **88**, 122506, (2006).
[38] V. V. Laguta, T. V. Antimirova, M. D. Glinchuk, I. P. Bykov, J. Rosa, M. Zaritskii, L. Jastrabík, L. Soukup, Y. Wanzong, Z. Jianrong, and L. Gaomin, J. Korean Phys. Soc. **32**, 5700 (1998).
[39] E. Siegel and K. A. Müller, Phys. Rev. B **19**, 109 (1979).
[40] D. J. Newman, J. Siegel **9**, 4285 (1976).
[41] E. Erdem, R. Böttcher, H. C. Semmelhack, H. J. Gläsel, and E. Hartmann, Phys. Status Solidi B **239**, R7 (2003).
[42] T. J. Yang, V. Gopalan, P. J. Swart, and U. Mohideen, Phys. Rev. Lett. **82**, 4106 (1999).
[43] D. Damjanovic, Rep. Prog. Phys. **61**, 1267 (1998).
[44] G. E. Pike, W. L. Warren, D. Dimos, B. A. Tuttle, R. Ramesh, J. Lee, V. G. Keramidas, and J. T. Evans, Appl. Phys. Lett. **66**, 484 (1995).
[45] S. Pöykkö and D. J. Chadi, Phys. Rev. Lett. **83**, 1231 (1999).
[46] D. C. Lupascu, *Fatigue in Ferroelectric Ceramics and Related Issues* (Springer, Heidelberg, 2004).
[47] A. K. Tagantsev, I. Stolichnov, E. L. Colla, and N. Setter, J. Appl. Phys. **90**, 1387 (2001).
[48] B. Güttler, U. Bismayer, P. Groves, and E. Salje, Semicond. Sci. Technol. **10**, 245 (1995).
[49] Such calculations are currently performed in collaboration with the group of P. C. Schmidt (TU Darmstadt).